I&EC research
Industrial & Engineering Chemistry Research

Article

pubs.acs.org/IECR

Mathematical Modeling of a Dip-Coating Process Using a Generalized Newtonian Fluid. 2. Model Validation and Sensitivity Analysis

Juan M. Peralta,* Bárbara E. Meza, and Susana E. Zorrilla

Instituto de Desarrollo Tecnológico para la Industria Química (INTEC), Universidad Nacional del Litoral—CONICET, Güemes 3450, Santa Fe, S3000GLN, Argentina

ABSTRACT: Dip coating is a simple, straightforward, and economical technique used in many food industrial applications. The objective of this work was to validate a mathematical model (presented by the authors in a companion paper as Part 1) of the fluid-dynamic variables in a dip-coating process considering that the film-forming fluid behaves as a generalized Newtonian fluid, with data obtained from literature, and to perform a sensitivity analysis. A validation process was carried out using experimental data of average film thickness of different film-forming fluids (commercial milk chocolate, commercial deep-fat frying batters, glycerol/water solutions, sugar/syrup solutions, glycerine/water solutions, mineral oil, and Carbopol solutions). On the basis of the low errors obtained, predictions were considered satisfactory. An extensive examination of the effect of the main process variables, such as τ_0, K, n, m, U_p, ρ, θ and h, on the velocity profile and the characteristics of the local and average film thickness was established.

1. INTRODUCTION

Dip coating is a simple, straightforward, and economical technique used in many industrial applications.[1] The objective of this procedure is to obtain a film of nonvolatile solutes deposited on the solid substrate surface. The dip-coating process involves several steps: the immersion of the substrate into a bath containing the film-forming fluid, the withdrawal of the substrate from the reservoir, and the draining of the film-forming fluid by gravity.[2] In both withdrawal and draining steps, secondary events like evaporation of solvent and concentration of solutes, that complete the film formation, are expected.[3−5] However, if the coating process can take place under isothermal and non-evaporative conditions, like in many practical situations, the problem reduces to the study of the fluid dynamic of the system.[2]

The rheological behavior of the film-forming fluid has been taken into account during the analysis and design of the dip-coating technique and also during the mathematical description of the transport phenomena of dip-coating processes used in polymer and food industrial applications.[5−9] Several experimental and theoretical studies of the dip-coating process, considering only the withdrawal step and fluids with Newtonian and non-Newtonian behavior, have been published. For example, Spiers et al.[10] and Kizito et al.[11] studied a continuous withdrawal system using Newtonian film-forming fluids such as glycerol/water, lubricating oils, sugar syrup/water, and silicon oils. Spiers et al.[12] and Adachi et al.[13] modeled theoretically a dip-coating process considering only a continuous withdrawal step and using fluids with power-law and viscoelastic behavior, like Carbopol/water and polyacrylamide/water solutions. Similarly, several works have been done considering only the draining step as a priority of the dip-coating process. Wichchukit et al.[14] and Karnjanolarn and McCarthy[15] modeled and simulated numerically the drainage of milk chocolate melt using a dip-coating method taking into account that the rheological behavior of the material was described by the Casson model.[16] In those studies, good theoretical and experimental agreement was obtained for film thickness values.

In a recent work, a theoretical study of the fluid dynamic phenomena in a dip-coating process, considering both withdrawal and draining steps and that the film-forming fluid behaves as generalized Newtonian fluid (GNF), was performed.[17] It is important to recall that the GNF is an extension of the Newtonian fluid that incorporates the shear-rate-dependent viscosity without taking into account time-dependent elastic effects and normal stress.[18] Peralta et al.[17] obtained their model using rigorous momentum and mass balances that were applied to a monophasic, isothermal, and non-evaporative system, while the main forces are viscous and gravitational. The model was solved analytically and the obtained expressions can be used to predict the principal process variables in both withdrawal and drainage stages (velocity profile, flow rate, local and average film thickness, etc.). It is important to mention that the rheological model adopted by Peralta et al.[17] includes other several important rheological models (besides the generalized Herschel−Bulkley) such as the Heinz−Casson,[19] Casson,[16] Mizrahi−Berk,[20] Herschel−Bulkley,[21] Ostwald−de Waele,[22] Bingham,[23] and Newtonian models.

To complete a theoretical study, experimental validation and sensitivity analysis of the mathematical models are used in the literature. Experimental validation, where the principal process variables are experimentally obtained in strict controlled conditions, is always mandatory for testing the accuracy of theoretical results obtained with the model.[24,25] In addition, sensitivity analysis allows testing the range of validity of the equations, giving the possibility to analyze how the variation of

Received: January 28, 2014
Revised: March 18, 2014
Accepted: March 20, 2014
Published: March 20, 2014

   dx.doi.org/10.1021/ie500408f | *Ind. Eng. Chem. Res.* 2014, 53, 6533−6543

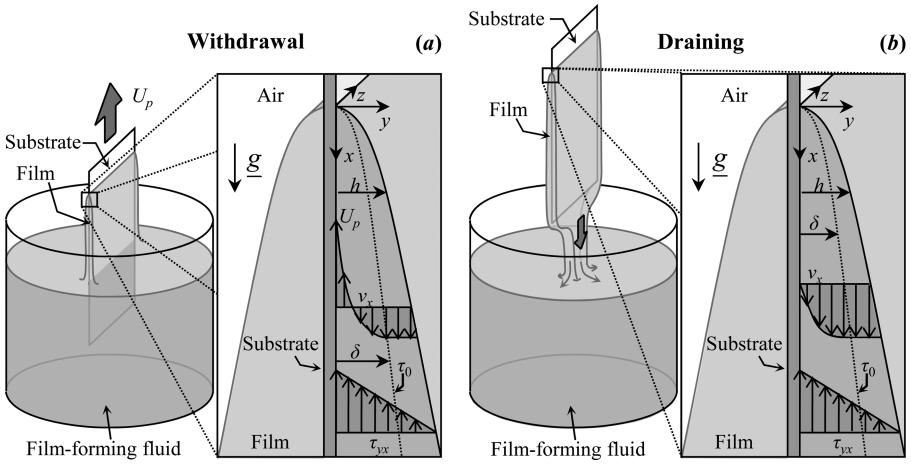

Figure 1. Schematic diagram of dip-coating process.

parameters affects the behavior of the theoretically predicted values obtained with the model.[26,27] Therefore, the objective of this work was to validate the model (and in addition to validate the other rheological models involved) developed by Peralta et al.[17] with experimental data obtained from literature and to perform a sensitivity analysis of the main parameters.

2. THEORETICAL APPROACH

2.1. Studied System and Mathematical Model. The expressions of the mathematical model used in the present work were obtained in a companion paper.[17] The mathematical model estimates the fluid-dynamic variables of a dip-coating process, taking into account that the main forces driving the process are gravitational (as an external influence) and viscous forces (as an internal influence). Surface phenomena (i.e., surface tension) were neglected. The dip-coating process variables were estimated by assuming that the film-forming fluid can be regarded as a generalized Newtonian fluid:[18,28]

$$\underline{\underline{\tau}} = -\eta\underline{\underline{\dot{\gamma}}} \tag{1}$$

where $\underline{\underline{\tau}}$ is the shear stress tensor [Pa], $\underline{\underline{\dot{\gamma}}}$ is the rate of deformation tensor (i.e., shear rate tensor) [s^{-1}], $\eta = f(|\underline{\underline{\dot{\gamma}}}|, T, p, C)$ is the apparent viscosity (scalar quantity) [Pa s], $|\underline{\underline{\dot{\gamma}}}|$ is the second invariant or magnitude of $\underline{\underline{\dot{\gamma}}}$ [s^{-1}], T is the temperature [K], p is the thermodynamic pressure [Pa], and C is the concentration [kg m^{-3}].

The rheological model for η was proposed by Ofoli et al.[29] as a generalization of the 3 parameter Herschel–Buckley model for inelastic fluid foods by adding a fourth parameter to yield:

$$\eta = (\tau_0^m |\underline{\underline{\dot{\gamma}}}|^{-m} + K^m |\underline{\underline{\dot{\gamma}}}|^{n-m})^{1/m} \tag{2}$$

where $\tau_0 = f_1(T, p, C)$ is the yield stress [Pa], $k = f_2(T, p, C)$ is the consistency index [Pa $s^{n/m}$], and $n = f_3(T, p, C)$ and $m = f_4(T, p, C)$ are dimensionless coefficients.

The analytical nature of the model leads to an expression for each variable that is a function of the operative parameters. Taking into account the amount of variables and the related equations that can be considered, only a selected set of expressions applied to certain conditions was studied. Those conditions were chosen based on the main stages that could be described in a dip-coating process (Figure 1): (1) the substrate is withdrawn from the coating fluid as the film is draining (i.e. withdrawal or lifting stage), and (2) the substrate is static and the film is drained (i.e., draining or removing stage).[2,30]

2.1.1. Velocity Profile for the Withdrawal Stage. The velocity profile for the withdrawal of a plate from the bath that contains the coating liquid can be estimated by the following.[17]

For $0 \le y \le \delta$:

$$\frac{v_x}{U_p} \cong \frac{n}{(n+1)m} S_K^{-m/n}[\psi(0) - \psi(y)] - 1 \tag{3}$$

For $y > \delta$:

$$\frac{v_{x,y\ge\delta}}{U_p} \cong \frac{n}{(n+1)m} S_K^{-m/n}\psi(0) - 1 \tag{4}$$

where

$$\psi(y) = \left(1 - \frac{y}{h}\right)^{m/n+1}\left\{1 - \left\{\frac{S_{\tau_0}}{[1-(y/h)]}\right\}^m\right\}^{(n+1)/n} {}_2F_1\left\{1, 1 - \frac{1}{m}; 2 + \frac{1}{n}; 1 - \left\{\frac{S_{\tau_0}}{[1-(y/h)]}\right\}^m\right\} \tag{5}$$

$$\psi(0) = (1 - S_{\tau_0}^m)^{(n+1)/n} {}_2F_1\left(1, 1 - \frac{1}{m}; 2 + \frac{1}{n}; 1 - S_{\tau_0}^m\right) \tag{6}$$

$$S_{\tau_0} = \frac{\text{yield stress}}{\text{maximum stress}} = \frac{\tau_0}{\rho g_x h} \tag{7}$$

$$S_K = \frac{\text{viscous stress}}{\text{maximum stress}} = \frac{K(U_p/h)^{n/m}}{\rho g_x h} \tag{8}$$

$$\delta = h - \tau_0/(\rho g_x h) \tag{9}$$

where v_x is the velocity component in x direction [m s^{-1}], U_p is the plate velocity [m s^{-1}], y is the position in the y direction [m], h is the local thickness of the film at x [m], ${}_2F_1[a, b; c; s]$ is the Gauss hypergeometric function [−], ρ is the density of the film [kg m^{-3}], and g_x is the component of the gravity vector in the x direction (9.81) [m s^{-2}] and can be related to the angle between the axis of the plate and the axis of $\underline{g}$ (θ):

$$g_x = |\underline{g}| \cos(\theta) \tag{10}$$

dx.doi.org/10.1021/ie500408f | Ind. Eng. Chem. Res. 2014, 53, 6533−6543

2.1.2. Velocity of the Plate When the Net Flux Is Zero (Q_z = 0). The effect of the velocity of the plate on the film thickness and the operative parameters, with the flow rate of the film conveniently equated to zero, can be estimated by[17]

$$U_p \cong \frac{n}{(n+1)m}\left(\frac{\rho g_x h^{n/m+1}}{K}\right)^{m/n}(1 - S_{\tau_0}^m)^{(n+1)/n} \; {}_2F_1\left(1, 1 - \frac{2}{m}; 2 + \frac{1}{n}; 1 - S_{\tau_0}^m\right) \quad (11)$$

2.1.3. Ratio of Average Velocity to Maximum Velocity for the Draining Stage (U_p = 0). One of the quantities that are usually estimated when the theoretical velocity profile is known for a given system is the ratio of the average velocity to the maximum velocity of the fluid. This parameter can be estimated from the ratio of the average velocity to the velocity of the solid fraction of the film[17] (or surface velocity) when the velocity of the plate is zero (U_p = 0, that is, $v_{x,y\geq\delta} = v_{x,\max}$). In this case:

$$\frac{\langle v_x\rangle_y}{v_{x,\max}} \cong \frac{{}_2F_1\left(1, 1 - \frac{2}{m}; 2 + \frac{1}{n}; 1 - S_{\tau_0}^m\right)}{{}_2F_1\left(1, 1 - \frac{1}{m}; 2 + \frac{1}{n}; 1 - S_{\tau_0}^m\right)} \quad (12)$$

where $\langle v_x\rangle_y$ is the average of the velocity component in x direction of the film (averaged in the y direction) [m s^{-1}] and $v_{x,\max}$ is the maximum velocity component in x direction of the film [m s^{-1}].

2.1.4. Local Film Thickness for the Draining Stage (U_p = 0). The local film thickness that is being drained from a static plate (U_p = 0) can be estimated by[17]

$$\left(\frac{\rho g_x h}{K}\right)^m - \left(\frac{\tau_0}{K}\right)^m - \left(\frac{x}{ht}\right)^n \cong 0 \quad (13)$$

2.1.5. Average Film Thickness for the Draining Stage (U_p = 0). The homogeneity can be considered an important attribute in a coating process for certain conditions. This characteristic can be estimated from the ratio of the average film thickness to the local film thickness. That is, the higher the mentioned ratio is, the more uniform is the thickness of the film. Thus, conveniently equating the plate velocity to zero (U_p = 0) (*i.e.*, draining or removing stage), the ratio can be estimated by[17]

$$\frac{\langle h\rangle_x}{h} \cong {}_2F_1\left(1, -\frac{2}{m}; \frac{1}{n} + 1; 1 - S_{\tau_0}^m\right) + \frac{n}{m(n+1)}(1 - S_{\tau_0}^m)\,{}_2F_1\left(1, 1 - \frac{2}{m}; \frac{1}{n} + 2; 1 - S_{\tau_0}^m\right) \quad (14)$$

where $\langle h\rangle_x$ is the average of the local film thickness in the x direction [m].

2.2. Experimental Validation. A validation process was carried out using experimental data of average film thickness obtained from literature. The experimental data correspond to coating films developed under conditions with different values of U_p (*i.e.*, withdrawal and draining stages). The data with $U_p > 0$ and $U_p = 0$ were compared with eqs 11 and 14, respectively. The information used to validate the mathematical model, with the corresponding physical properties of the film-forming fluids, is shown in Tables 1 and 2. A total of 159 experimental data corresponding to average film thickness of several food products and food ingredients (commercial milk chocolate, commercial deep-fat frying batters, glycerol/water solutions, sugar/syrup solutions, and glycerine/water solutions), mineral oil, and 0.16%

Table 1. Experimental Data of Dip-Coating Processes Obtained from Literature and Used for Validation (θ = 0°)

film-forming fluid	rheological behavior	U_p [m s^{-1}]	Q_z [m^2 s^{-1}]	$\langle h\rangle_x$ [mm]	t_d [s]	range *Ca*	description	ref
commercial milk chocolate	non-Newtonian	not applicable	not applicable	0.6–4.6 (22 data by triplicate)	20	not applicable	samples with two granulometry (14 and 28 μm), two emulsifiers (lecithin and polyglycerol polyricinoleate), and six concentrations of emulsifier (0.0–0.5%); substrate: acrylic plate (L = 44.5 mm)	15
commercial deep-fat frying batters	non-Newtonian	not applicable	not applicable	0.2–2.0 (39 data by one replicate)	60–120	not applicable	samples with different percentage of solid contents (43.8–57.1%); substrate: polymethyl methacrylate plate (L = 40 mm)	36
glycerol/water	Newtonian	2.3×10^{-3}–4.4×10^{-1}	1.6×10^{-7}–1.3×10^{-3}	0.1–3.3 (66 data by duplicate)	not applicable	0.007–6.1	different solutions of glycerol/water	37
sugar/syrup	Newtonian	2.1×10^{-3}–3.9×10^{-1}	1.3×10^{-6}–1.1×10^{-4}	0.7–3.2 (6 data by duplicate)	not applicable	0.2–4	Solution of sugar/syrup	37
glycerine/water	Newtonian	2.5×10^{-2}–1.8×10^{-1}	5.5×10^{-6}–1.1×10^{-4}	0.2–0.8 (6 data by triplicate)	not applicable	0.05–0.35	solution of glycerine/water	35
mineral oil	Newtonian	1.2×10^{-2}–1.4×10^{-1}	2.5×10^{-6}–1.2×10^{-4}	0.2–1.0 (6 data by triplicate)	not applicable	0.06–0.68	mineral oil	35
mineral oil	Newtonian	3.4×10^{-3}–3.2×10^{-2}	6.3×10^{-7}–5.1×10^{-5}	0.2–2.0 (8 data by quadruplicate)	not applicable	0.03–2.34	mineral oil with different viscosities	30
Carbopol	non-Newtonian	8.1×10^{-3}–5.0×10^{-1}	7.8×10^{-7}–3.6×10^{-4}	0.1–0.8 (6 data by triplicate)	not applicable	0.01–0.31	solution of 0.16% Carbopol	35

dx.doi.org/10.1021/ie500408f | *Ind. Eng. Chem. Res.* 2014, 53, 6533–6543

Table 2. Physical Properties of Film-Forming Fluids Obtained from Literature and Used in the Validation Process

film-forming fluid	GNF model parameters	rheological parameters	$\lvert\underline{\dot{\gamma}}\rvert$ [s^{-1}]	ρ [kg m^{-3}]	σ [N m^{-1}]	ref
commercial milk chocolate	$n = m = 1/2$ (Casson model)	τ_0 = 0−34.8 Pa K = 1.49−11.0 Pa $s^{1/2}$	2−50	1216−1227	unknown	15
commercial deep-fat frying batters	$m = 1$, $\tau_0 = 0$ (Ostwald−de Waele model)	n = 0.54−0.75 K = 1.71−68.09 Pa s^n	0.16−50	1070−1200	unknown	36
glycerol/water	$n = m = 1$, $\tau_0 = 0$ (Newtonian model)	η = 0.13−1.05 Pa s	not applicable	1215−1257	0.0629−0.066	37
sugar/syrup	$n = m = 1$, $\tau_0 = 0$ (Newtonian model)	η = 8.4 Pa s	not applicable	1385	0.08	37
glycerine/water	$n = m = 1$, $\tau_0 = 0$ (Newtonian model)	η = 0.103 Pa s	not applicable	1220	0.0525	35
mineral oil	$n = m = 1$, $\tau_0 = 0$ (Newtonian model)	η = 0.16 Pa s	not applicable	880	0.0317	35
mineral oil	$n = m = 1$, $\tau_0 = 0$ (Newtonian model)	η = 0.288−2.42 Pa s	not applicable	830−894	0.032−0.0335	30
Carbopol	$m = 1$, $\tau_0 = 0$ (Ostwald−de Waele model)	n = 0.56 K = 0.601 Pa s^n	unknown	1000	0.0577	35

Carbopol solutions were used to compare with the model predictions.

3. RESULTS AND DISCUSSION

3.1. Model Validation. Figure 2 shows the comparison between the experimental and theoretical average film thickness

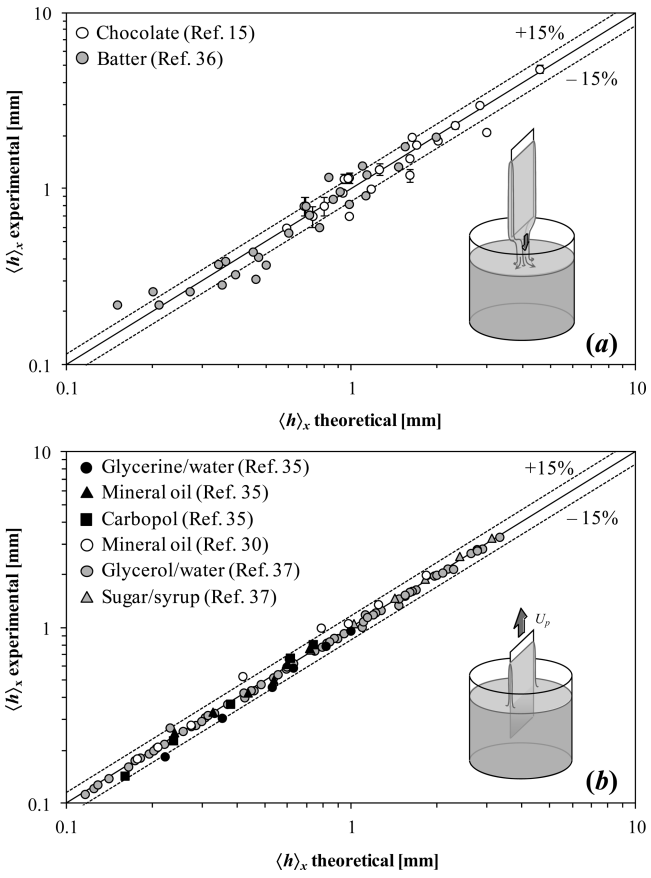

Figure 2. Comparison between the experimental average film thickness ($\langle h\rangle_x$ experimental) obtained from literature and the theoretical average film thickness ($\langle h\rangle_x$ theoretical) estimated using (*a*) eq 14 (draining) and (*b*) eq 11 (withdrawal).

for $U_p = 0$ (Figure 2*a*) and $U_p > 0$ (Figure 2*b*). In the case of draining (Figure 2*a*), the root mean squared error (rmse) estimated by eq 15 was 0.1 mm for a range of 0.2 mm < $\langle h\rangle_x$ < 4.6 mm. On the other hand, when $U_p > 0$ (*i.e.*, withdrawal stage), the rmse was lower than 0.1 mm for a range of 0.1 mm < $\langle h\rangle_x$ < 3.2 mm. These errors were considered very low. On the basis of the obtained errors, the heterogeneity of the film-forming fluids, and the different experimental conditions, model predictions were considered as very good.

$$\text{rmse} = \sqrt{\frac{1}{N}\sum_{i=1}^{N}(\langle h\rangle_x \text{ theoretical} - \langle h\rangle_x \text{ experimental})^2} \tag{15}$$

It should be pointed out that eq 11 can have several roots depending on the value of n and m. For example, for Newtonian behavior, the model may provide two positive and one negative real roots as it was observed by Van Rossum.[25] For the cases studied, eq 11 resulted in multiple positive and negative real and complex roots. Taking into account physical reasons, negative real roots and complex roots were discarded. In all cases, the lowest real roots obtained using eq 11 were used because they have the best fit with the experimental data. The error of considering the second lowest real root was in the order of 100% (data not shown). The smallest error obtained using the lowest real root may be explained considering that a thinner film has less potential energy than a thicker one. Therefore, if a perturbation is applied to the system when it has a theoretically possible thicker film, the system could jump to a more stable condition (i.e., lower potential energy) associated with the lowest theoretically possible film thickness for that condition. In other words, a reduction of thickness would mean a minimization of the internal energy of the system in accordance with the second law of thermodynamics.[31]

3.2. Model Sensitivity Analysis. A sensitivity analysis was performed to assess the effect of varying parameters in the mathematical model on the main predicted variables.

3.2.1. Velocity Profile. In Figure 3, the velocity profile (v_x/U_p) in the film as function of the relative position $\tilde{y}$ for different values of the dimensionless parameters is observed. This figure shows that an increase in S_K (i.e., increase in K, U_p, n and a decrease in ρ, θ, h_L, and m) produces a less gradual velocity profile originating a delay in the fluid descent (Figure 3*a*). For $S_K \to \infty$, the profile will be flat and equal to the plate velocity (i.e., solid behavior) and a profile with $v_x/U_p \to -\infty$ is expected for $S_K = 0$ (i.e., fluid without resistance to flow). In addition, the relative influence of S_K on v_x/U_p is major for $S_K < 0.1$. For $S_K > 0.1$, the viscous resistance is such that the influence of S_K is not transferred to v_x/U_p and the profiles are more uniform in the y direction. On the other hand, the effect of S_{τ_0} can be observed in Figure 3b. For $S_{\tau_0} = 0$ (i.e., fluid with $\tau_0 \to 0$), the model produces a viscous velocity profile. As S_{τ_0} increases, a solidlike layer starts to grow in the film (flat portion of the velocity profiles). In that region, which grows

dx.doi.org/10.1021/ie500408f | Ind. Eng. Chem. Res. 2014, 53, 6533−6543

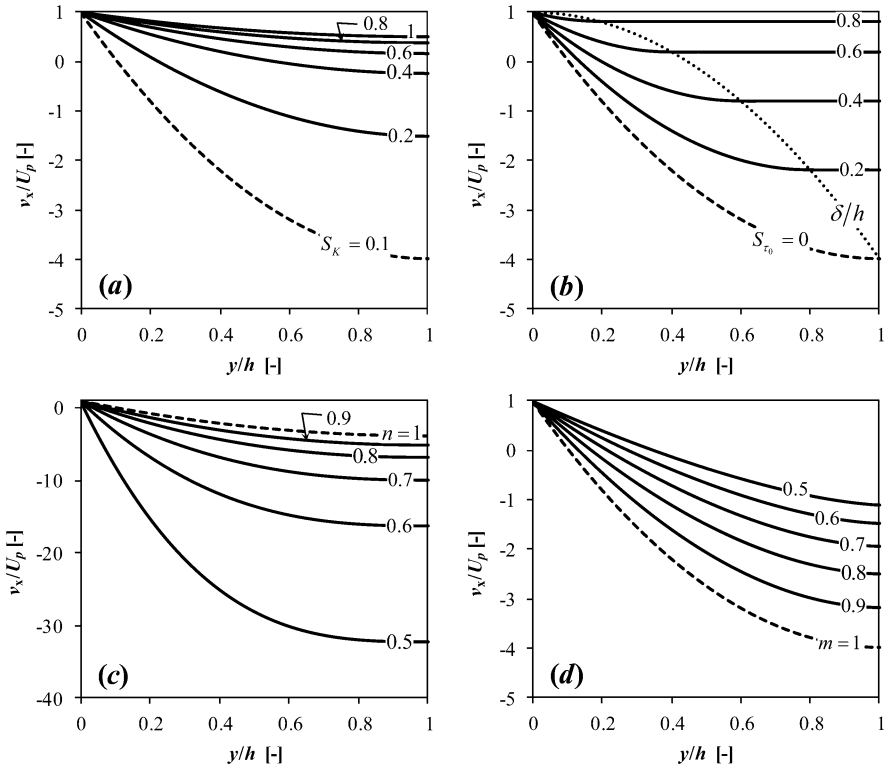

Figure 3. Ratio of the velocity component in the x direction to the plate velocity v_x/U_p as a function of the non-dimensional position y/h for different values of (*a*) S_K, (*b*) S_{τ_0}, (*c*) n, and (*d*) m. The condition adopted as reference is represented by a dashed line and has the values of $n = m = 1$, $S_K = 0.1$ and $S_{\tau_0} = 0$ (i.e., Newtonian behavior). The dotted line in (*b*) represents the threshold between the viscous and solid behavior inside the film.

from the film-air interface, the shear exerted on the molecules are smaller than the yield stress τ_0. In addition, as $S_{\tau_0} \to 1$, the yield stress tends to be the maximum stress in the system. This means that the shear stress generated in the system cannot produce flow and the film behaves as a solid material (i.e., flat profile with $v_x/U_p \to 1$ in Figure 3b). The effect of n on v_x/U_p is shown in Figure 3*c*. First, the range of velocities increases as n decreases. This behavior can be explained because, for smaller values of n, the effect of the shear stress on the gradients increases, producing more negative velocity profiles. Second, as n increases, the velocity profiles tend to be more uniform and less affected by a change in n. In the case of $n \to \infty$, the shear stress loses influence on the velocity of deformations (i.e., velocity gradients) producing more uniform profiles. Finally, m shows an opposite effect on v_x/U_p compared to n. At the extremes, as $m \to 0$, the profiles become more uniform and vice versa.

3.2.2. Plate Velocity for the Withdrawal Stage with Zero Net Flow. Figure 4 shows the effect of the plate velocity on the local film thickness for different values of the system parameters (eq 11). As n decreases, a thinner film is formed. This is due to the effect of the gravity via the shear stress on the velocity gradients giving more fluidity to the film and consequently leaving less amount of material on the plate. At the extremes, as $n \to 0$, $h \to 0$ and vice versa. As for the velocity profiles (Figure 3), the effect of m on the plate velocity is the opposite to the effect shown by n. In this case, the greater the value of m is, the thinner is the film, and as $m \to \infty$, $h \to 0$. On the other hand, an increment in τ_0 produces thicker films for a given value of U_p. This occurs because the film has a fraction that behaves as a solid material that is added to the viscous layer and it is not deformable under the gravity effect. That is, lower values of U_p will be needed to produce a film with a certain thickness as τ_0 increases. This behavior was observed by Chambon et al.[32] In the case of K (Figure 4d), an increment in K (i.e., less resistance to flow) produces an increment in h for a given U_p. A similar behavior was observed by Tallmadge[33] for a power-law fluid. This means that for a certain value of h, the necessary value of U_p is smaller due to the reduced effect of the shear stress on the velocity gradients. Figure 4e shows that an increase in the film density causes a thinner film for a given U_p. This is because a denser film has more mass per volume affected by the gravity. Finally, the greater the inclination of the plate with respect to the gravity vector is, the thicker is the film (Figure 4f). Taking into account the range of θ that can be used, this effect is smaller compared with the rest of the system parameters.

3.2.3. Ratio of the Average Velocity to the Maximum Velocity for the Draining Stage. The ratio of the average velocity to the maximum velocity (when the plate is static) as a function of S_{τ_0} for different combinations of n and m is shown in Figure 5. In all cases, it is important to mention that the profiles are independent of the position, K, and time. First, Figure 5*a* shows linear profiles for different values of n with $m = 1$ (i.e., Herschel−Bulkley case). These profiles are bounded in the range $^1/_2 \le \langle v_x \rangle_y / v_{x,\max} \le 1$. The case of $\langle v_x \rangle_y / v_{x,\max} \to {}^1/_2$ is explained by assuming that the fluid has no yield stress ($\tau_0 \to 0$) and the fluidity is at maximum ($n \to \infty$) obtaining a linear velocity profile. Also, as $S_{\tau_0} \to 0$, the values of $\langle v_x \rangle_y / v_{x,\max}$ tend to $\langle v_x \rangle_y / v_{x,\max} = (n+1)/(2n+1)$ (also found by Sylvester et al.[34]) and as S_{τ_0} approaches to 1, the values of $\langle v_x \rangle_y / v_{x,\max}$ tend to 1. When $n \to \infty$, the values of $\langle v_x \rangle_y / v_{x,\max} \to (^1/_2)(S_{\tau_0} + 1)$ (dotted line in Figure 5a). In addition, an increase in n causes a decrease in $\langle v_x \rangle_y / v_{x,\max}$. This is due to the reduced effect of the gravity over the velocity profiles (as a result of the increment of n) and therefore

dx.doi.org/10.1021/ie500408f | *Ind. Eng. Chem. Res.* 2014, 53, 6533−6543

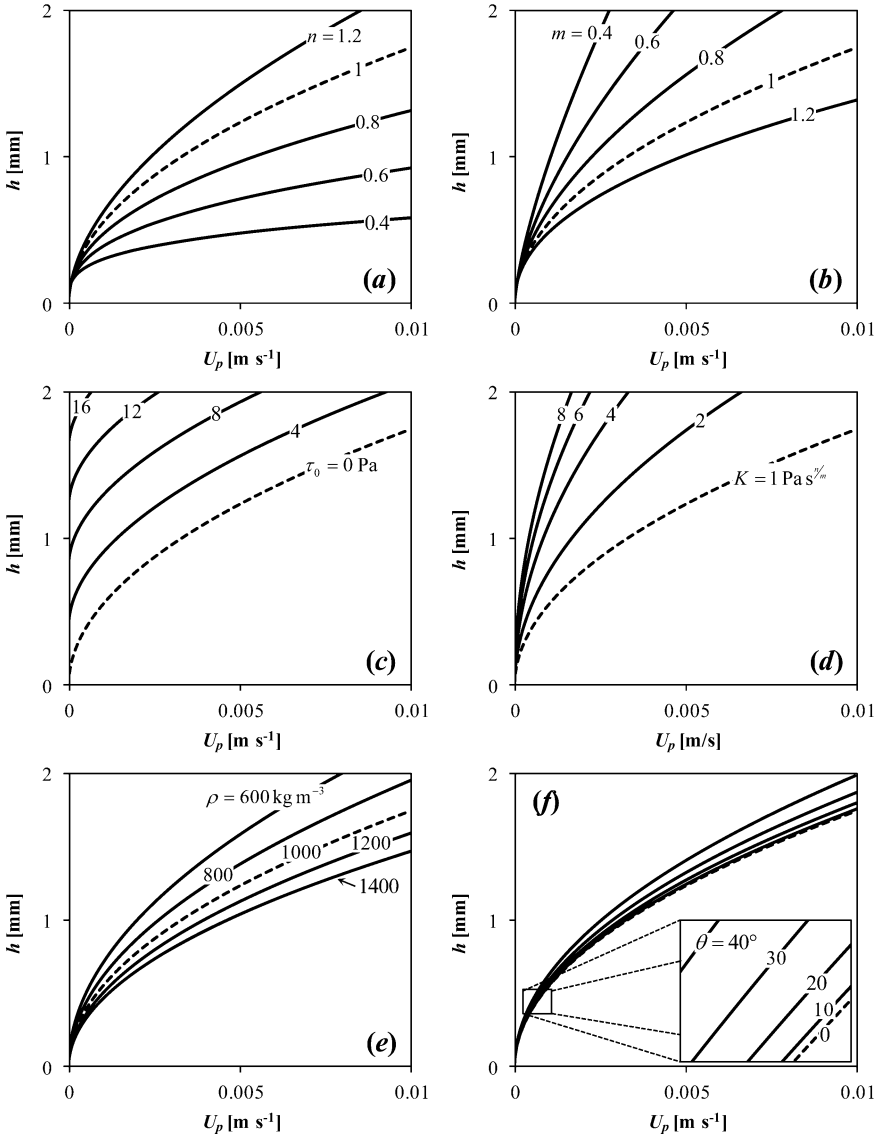

Figure 4. Local film thickness h as a function of the plate velocity U_p for different values of (*a*) n, (*b*) m, (*c*) τ_0, (*d*) K, (*e*) ρ, and (*f*) θ. The condition adopted as a reference and represented by a dashed line has the values of $n = m = 1$, $\tau_0 = 0$ Pa, $K = 1$ Pa s$^{n/m}$, $\rho = 1000$ kg m^{-3}, and $\theta = 0°$.

the deformation of the film. Furthermore, the effect of an increase in n on $\langle v_x\rangle_y/v_{x,max}$ is reduced as n increases. Second, the effect of m with $n = 1$ is shown in Figure 5b. Here, the profiles are predicted by eq 16 which was obtained from eq 12.

$$\frac{\langle v_x\rangle_y}{v_{x,max}} \cong \frac{(m+1)}{2(m+2)}\frac{[2+(mS_{\tau_0}^2 - m - 2)S_{\tau_0}^m]}{[1+(mS_{\tau_0} - m - 1)S_{\tau_0}^m]} \quad (16)$$

Again the profiles are bounded in the range $1/2 \le \langle v_x\rangle_y/v_{x,max} \le 1$ and as S_{τ_0} approaches to 1, the values of $\langle v_x\rangle_y/v_{x,max}$ tend to 1. However, as $S_{\tau_0} \to 0$, the $\langle v_x\rangle_y/v_{x,max} \to (m+1)/(m+2)$. In this case, an increase in m produces an increase in $\langle v_x\rangle_y/v_{x,max}$. This effect is observed for small values of S_{τ_0}. In contrast, as S_{τ_0} increases, all the profiles tend to a line with a slope of $^1/_3$. At the extremes, as m approaches to zero, the values of $\langle v_x\rangle_y/v_{x,max} \to [1 - S_{\tau_0}^2 + 2\ln(S_{\tau_0})][4 - 4S_{\tau_0} + 4\ln(S_{\tau_0})]^{-1}$ (dotted line in Figure 5b). This last expression can be seen as a theoretical minimum boundary because m cannot adopt negative values. Third, Figure 5c shows the effect of $m = n$ (i.e., Heinz–Casson case) on the profiles of $\langle v_x\rangle_y/v_{x,max}$ as a function of S_{τ_0}. These profiles are bounded in the range of $^2/_3 \le \langle v_x\rangle_y/v_{x,max} \le 1$. For any value of m, as S_{τ_0} approaches to zero, $\langle v_x\rangle_y/v_{x,max} \to {}^2/_3$ and to 1 as $S_{\tau_0} \to 1$. In this case, a decrease in m produces an increase in $\langle v_x\rangle_y/v_{x,max}$. When $m < 1$, the profiles are concave, and conversely, convex profiles are observed when $m > 1$. A straight line, represented by a dashed line, is obtained for $m = 1$ (i.e., Bingham case). Also, as m increases, the effect of m on $\langle v_x\rangle_y/v_{x,max}$ is reduced. Finally, there is the case of the effect of n when $m = {}^1/_2$ (i.e., Mizrahi–Berk case) on $\langle v_x\rangle_y/v_{x,max}$. As in the first two cases, the profiles are bounded in the range $^1/_2 \le \langle v_x\rangle_y/v_{x,max} \le 1$. For any value of n, as $S_{\tau_0} \to 0$ the profiles $\langle v_x\rangle_y/v_{x,max} \to (2n+1)/(4n+1)$. Again, as in the first case (Figure 5a), an increase in n causes a decrease in $\langle v_x\rangle_y/v_{x,max}$ and this effect is reduced as n increases. At the extremes, as $n \to \infty$ the profiles $\langle v_x\rangle_y/v_{x,max} \to ({}^1/_2)(S_{\tau_0} + 1)$ (dotted line in Figure 5d) and tend to 1 as $n \to 0$. In this case, all profiles are concave.

3.2.4. Local Thickness Profiles for the Draining Stage. The effect of the position–time variable (x/t) on the local thickness

dx.doi.org/10.1021/ie500408f | *Ind. Eng. Chem. Res.* 2014, 53, 6533–6543

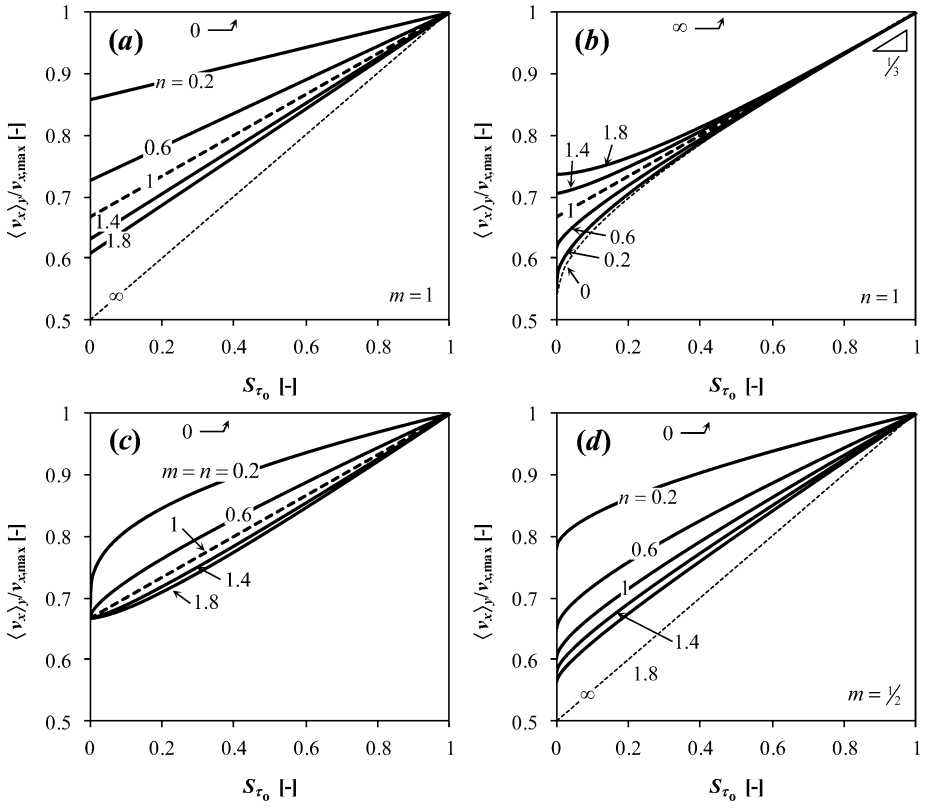

Figure 5. Ratio of the average velocity to the maximum velocity $\langle v_x\rangle_y/v_{x,max}$ as a function of S_{τ_0} for different values of (*a*) n (with $m = 1$) (i.e., Herschel−Bulkley case), (*b*) m (with $n = 1$), (*c*) $n = m$ (i.e., Heinz−Casson case) and (*d*) n (with $m = {}^1/_2$) (i.e., Mizrahi−Berk case). In panels *a*−*c*, the reference conditions were represented by a dashed line that correspond to a Bingham fluid (i.e., $n = m = 1$).

of the film is observed in Figure 6. This effect on h is similar to the one observed in Figure 4. In general, the profiles are monotonic and the local values of h always increase with an increment in x/t producing a concave function. Figure 6 panels a and b show that an increase in n and/or a decrease in m causes a decrease in h for a given x/t. As $n \to 0$ or $m \to \infty$, $h \to 0$ and vice versa. In the case of τ_0 (Figure 6c) and K (Figure 6d), an increase in those quantities produces and increase in h. More precisely, a change in τ_0 produces an approximately constant separation among the profiles of h with an extrapolated value of $h \to \tau_0(\rho g_x)^{-1}$ for $x \to 0$. On the other hand, a change in K causes scaled profiles of h. In general, the relative effect of K on h is greater than τ_0. This is because K affects $|\dot{\underline{\underline{\gamma}}}|$ (and consequently h) more directly than τ_0 (eq 13). Again, the smaller the density is (i.e., less effect of gravity due to a lighter film on the plate), the thicker is the thickness (Figure 6e). Finally, an increase in θ causes an increase in h because of a smaller effect of the gravity in the direction of the flow.

3.2.5. Average Thickness Profiles for the Draining Stage. Figure 7 shows the profiles of the average thickness $\langle h\rangle_x$ as a function of time for different values of the system parameters. In general, hyperbolic-type profiles are observed (i.e., $a + bt^{-c}$). It can be observed that an increase in n produces an increase in $\langle h\rangle_x$ for a given t (Figure 7a). This increment is greater for larger t and decreases as t increases. An inverse effect as a function of m is observed in Figure 7b. Here, an increase in m produces a decrease in $\langle h\rangle_x$ for a given t. As observed previously in the velocity profiles (Figure 3), an increase of n (or a decrease of m) reduces the effect of the shear stress (as a result of gravity) on the velocity gradients. Therefore, as time passes, the reduced amount of material on the plate causes the maximum shear of the system be reduced, and the changes in local and average thickness become smaller. Figure 7c shows that the asymptotic values of $\langle h\rangle_x$ are increased by an increment in τ_0. These values are predicted by $\langle h\rangle_{x,t\to\infty} = \tau_0(\rho g_x)^{-1}$. Also, for small values of t, $\langle h\rangle_x$ is less affected by a change in τ_0. The consistency index shows a proportional effect on $\langle h\rangle_x$ for a given time. This behavior could be explained by the fact that K affects directly $|\dot{\underline{\underline{\gamma}}}|$ compared to τ_0. Figure 7e shows that an increase of the film density causes a decrease in $\langle h\rangle_x$ for a given t. An increase in density means that there is more mass in the plate for a given volume that is affected by the gravitational field and as a result the draining of the fluid film is accelerated. Finally, a decrease in the angle of inclination of the plate with respect to the gravity vector (θ) causes a marginal increase in the average thickness of the film for a given time (Figure 7f).

3.2.6. Homogeneity of the Film Thickness. Figure 8 shows the ratio of the average thickness to the local thickness as a function of the non-dimensional shear stress S_{τ_0} for different values of the parameters. In all cases, monotonic increasing profiles of $\langle h\rangle_x/h$ are observed with an increase in S_{τ_0} (i.e., an increase in τ_0, a decrease in ρ, h, and in a less extent a decrease in θ). Moreover, in all cases, an independence of $\langle h\rangle_x/h$ with the position, K, and time was observed. The profiles are bounded in the range ${}^1/_2 \le \langle h\rangle_x/h \le 1$. This occurs because the local thickness of the film increases constantly with the position x (eq 13), making that $\langle h\rangle_x \le h$ for a given position. The value of $\langle h\rangle_x/h \to {}^1/_2$ is obtained because in the extreme case of $S_{\tau_0} = 0$ and $m \ll n$, h increases linearly with x (eq 13). The increase in S_{τ_0} produces a more homogeneous film thickness. This is because

dx.doi.org/10.1021/ie500408f | Ind. Eng. Chem. Res. 2014, 53, 6533−6543

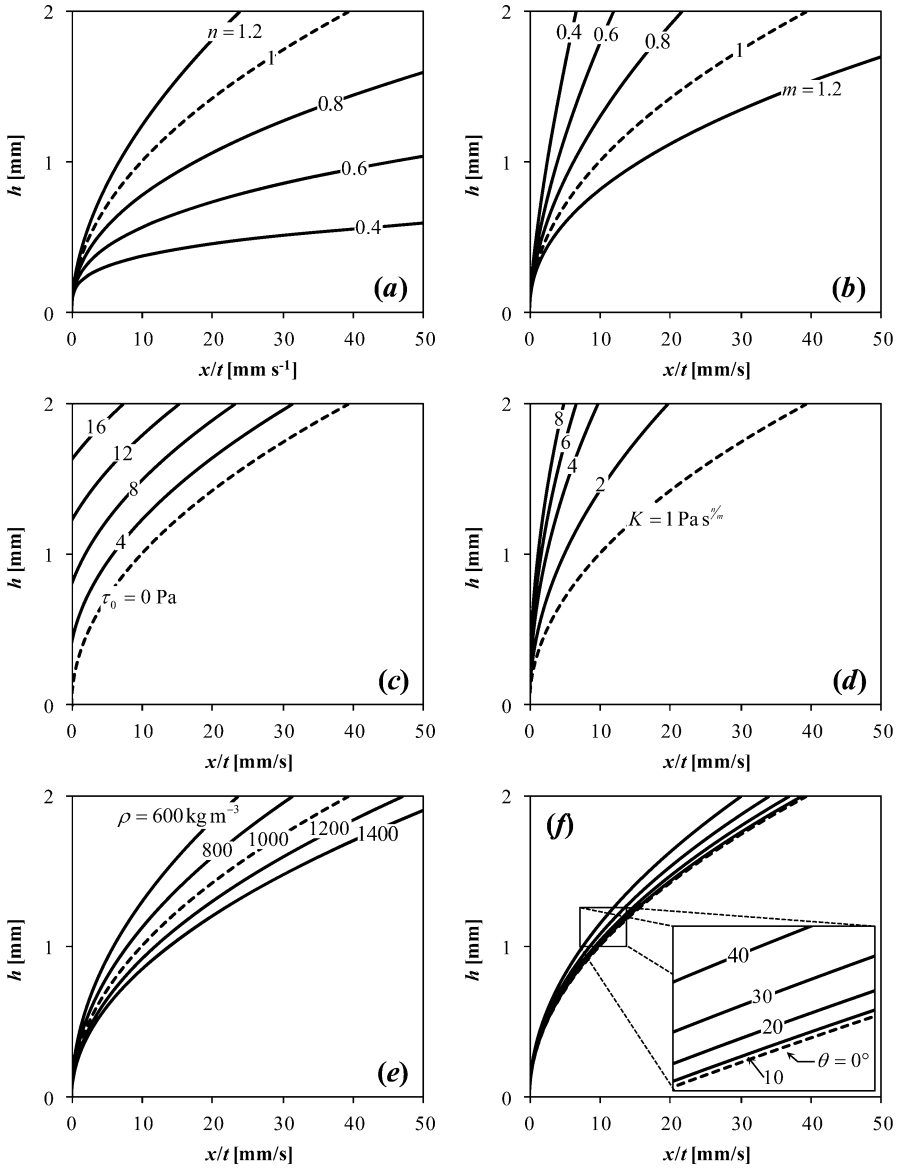

Figure 6. Local film thickness h as a function of time for different values of (*a*) n, (*b*) m, (*c*) τ_0, (*d*) K, (*e*) ρ, and (*f*) θ. The condition adopted as a reference and represented by a dashed line has the values of $n = m = 1$, $\tau_0 = 0$ Pa, $K = 1$ Pa $s^{n/m}$, $\rho = 1000$ kg m^{-3}, and $\theta = 0°$.

the fraction of the film that behaves as solid and is not deformable under gravitational forces occupies a larger portion of the film thickness. Figure 8a shows the profiles of $\langle h\rangle_x/h$ for a Herschel–Bulkley type material ($m = 1$). It is shown that a decrease in n produces an increase in $\langle h\rangle_x/h$ and more linear profiles for a given value of S_{τ_0}. On the other hand, an increase in n produces convex profiles with a minimum and maximum slopes at $S_{\tau_0} = 0$ and $S_{\tau_0} = 1$, respectively. At the extremes, when $n = 0$, the ratio $\langle h\rangle_x/h \to 1$ and when $n \to \infty$, the ratio $\langle h\rangle_x/h \to (^1/_2)(1 + S_{\tau_0}^2)$ (dotted line in Figure 8a). In eq 14 for $S_{\tau_0} \to 0$, the ratio $\langle h\rangle_x/h$ is predicted by $\langle h\rangle_x/h = (n + 1)/(2n + 1)$ (i.e., power law fluid). This result was also obtained by Gutfinger and Tallmadge.[35] The effect of m ($n = 1$) on $\langle h\rangle_x/h$ is shown in Figure 8b. In general, an increase in m produces an increase in $\langle h\rangle_x/h$ for a given value of S_{τ_0}. At $S_{\tau_0} = 0$, the ratio $\langle h\rangle_x/h$ can be estimated by $\langle h\rangle_x/h = [2(m + 1) - S_{\tau_0}^m(2 + m + mS_{\tau_0}^2)][2(m + 2)(1 - S_{\tau_0}^m)]^{-1}$ and at $S_{\tau_0} = 1$ the ratio $\langle h\rangle_x/h = 1$ with a slope of $^1/_2$ for any value of m. Similarly as in the previous case (Figure 8a), the slope of the profiles is a function of m, but as $S_{\tau_0} \to 1$, all the profiles tend to a slope of $^1/_2$. Low values of m produce concave profiles, and higher values of m produce convex profiles with a minimum slope at $S_{\tau_0} = 0$. At the extremes of m, when $m \to \infty$ the ratio $\langle h\rangle_x/h \to 1$, and when $m = 0$ the ratio can be estimated by $\langle h\rangle_x/h \to [2 \ln (S_{\tau_0}) + S_{\tau_0}^2 - 1][4 \ln (S_{\tau_0})]^{-1}$. Figure 8c shows the profiles of $\langle h\rangle_x/h$ as a function of S_{τ_0} when $n = m$ (i.e., fluid described with the Heinz–Casson model). The profiles begin with $\langle h\rangle_x/h = {}^2/_3$ and then the values of $\langle h\rangle_x/h$ increase at different rates as a function of m. For $m > 1$, the slope increases continuously as S_{τ_0} increases. On the other hand, for $m < 1$ the slope begins with a maximum and decreases as S_{τ_0} increases. Also, for $m < 1$ an increase in m produces a more pronounced change in $\langle h\rangle_x/h$ compared to the same increment in m for $m > 1$. Again, when $m = 0$, the ratio $\langle h\rangle_x/h \to 1$. Finally, Figure 8d shows the profiles of $\langle h\rangle_x/h$ vs S_{τ_0} for different values of n with $m = {}^1/_2$ (i.e., fluid described with the Mizrahi–Berk model). In general, the change of m from 1 (Figure 8*a*) to $^1/_2$

dx.doi.org/10.1021/ie500408f | Ind. Eng. Chem. Res. 2014, 53, 6533–6543

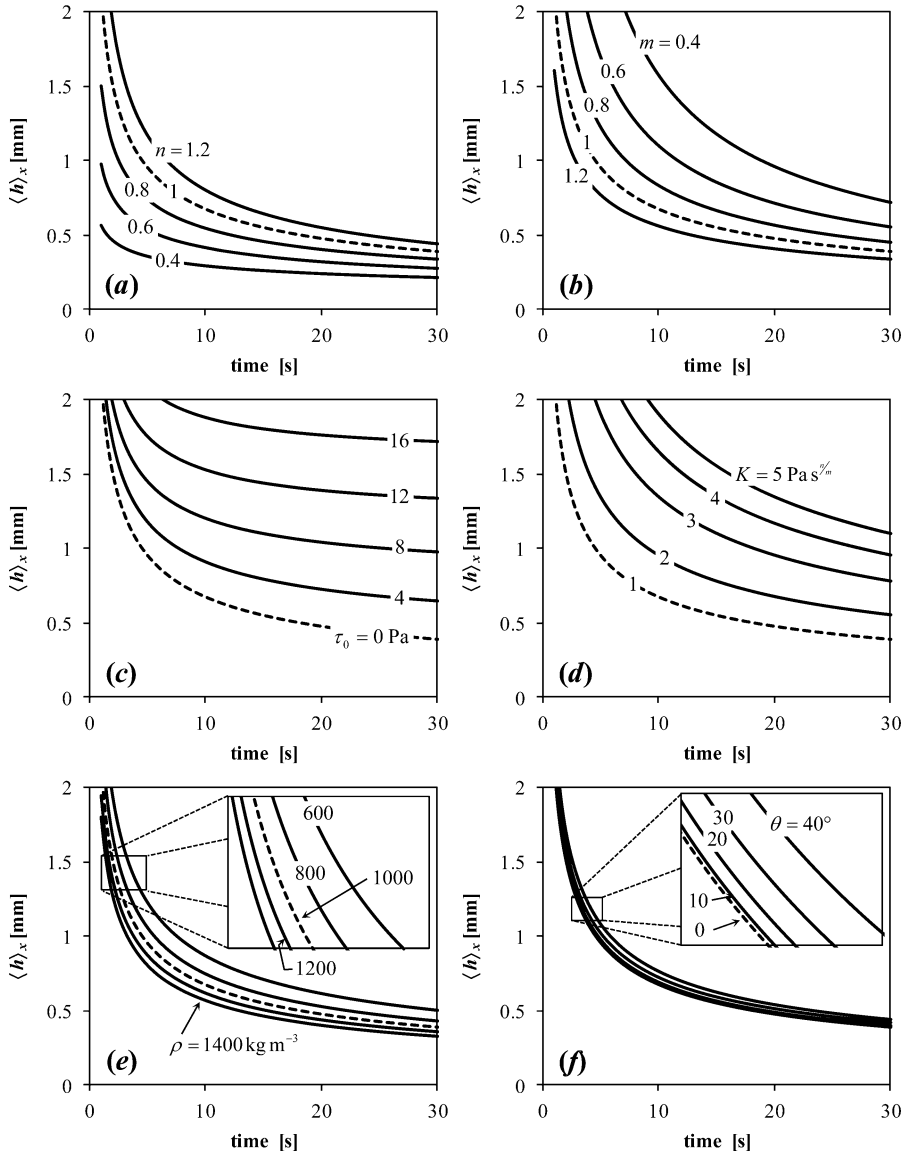

Figure 7. Average film thickness $\langle h \rangle_x$ as a function of time for different values of (*a*) n, (*b*) m, (*c*) τ_0, (*d*) K, (*e*) ρ, and (*f*) θ. The condition adopted as a reference and represented by a dashed line has the values $n = m = 1$, $\tau_0 = 0$ Pa, $K = 1$ Pa $s^{n/m}$, $\rho = 1000$ kg m^{-3}, and $\theta = 0°$.

produces more linear profiles for all values of n. The slopes show a maximum at $S_{\tau_0} = 0$ and rapidly decrease. An increment in n has the same effect as explained for the case of Figure 8a and at the extremes of n, when $n = 0$, the ratio $\langle h \rangle_x / h \rightarrow 1$ and when $n \rightarrow \infty$, the ratio $\langle h \rangle_x / h \rightarrow (^1/_2)(1 + S_{\tau_0}^2)$ (dashed line in Figure 8d).

4. CONCLUSIONS

In this study, validation and a sensitivity analysis of a mathematical model for the fluid-dynamic variables in a dip-coating process, considering that the film-forming fluid behaves as a GNF, were carried out. The model, based on the balance between the gravitational and viscous forces, was presented by the authors in a companion paper as Part 1.[17] The validation was performed using experimental data of averaged film thickness obtained from literature for different film-forming fluids (commercial milk chocolate, commercial deep−fat frying batters, glycerol/water solutions, sugar/syrup solutions, glycerine/water solutions, mineral oil, and 0.16% Carbopol solutions). Those materials presented different rheological behavior described as special cases of a GNF behavior. On the basis of the low errors obtained, the theoretical predictions of $\langle h \rangle_x$ were considered satisfactory. The sensitivity analysis was performed for withdrawal and draining stages. An extensive examination about the effect of the main process variables, such as τ_0, K, n, m, U_p, ρ, θ, and h on the velocity profile and the characteristics of the local and average film thickness were established. According to the obtained results, the developed model that was experimentally validated and sensitivity analyzed, presented several advantages such as theoretical nature, incorporation of a generalized rheological model that describes the behavior of the film-forming fluid, and an easy mathematical background. It is worth mentioning that this study is also valid for Heinz−Casson,[19] Casson,[16] Mizrahi−Berk,[20] Herschel−Bulkley,[21] Ostwald−de Waele,[22] Bingham,[23] and Newtonian models.

The proposed and validated model presented in this work (parts 1 and 2) may contribute to have a precise knowledge of the film-forming history and the film thickness profiles that is essential in food coating at the industrial scale.

dx.doi.org/10.1021/ie500408f | Ind. Eng. Chem. Res. 2014, 53, 6533−6543

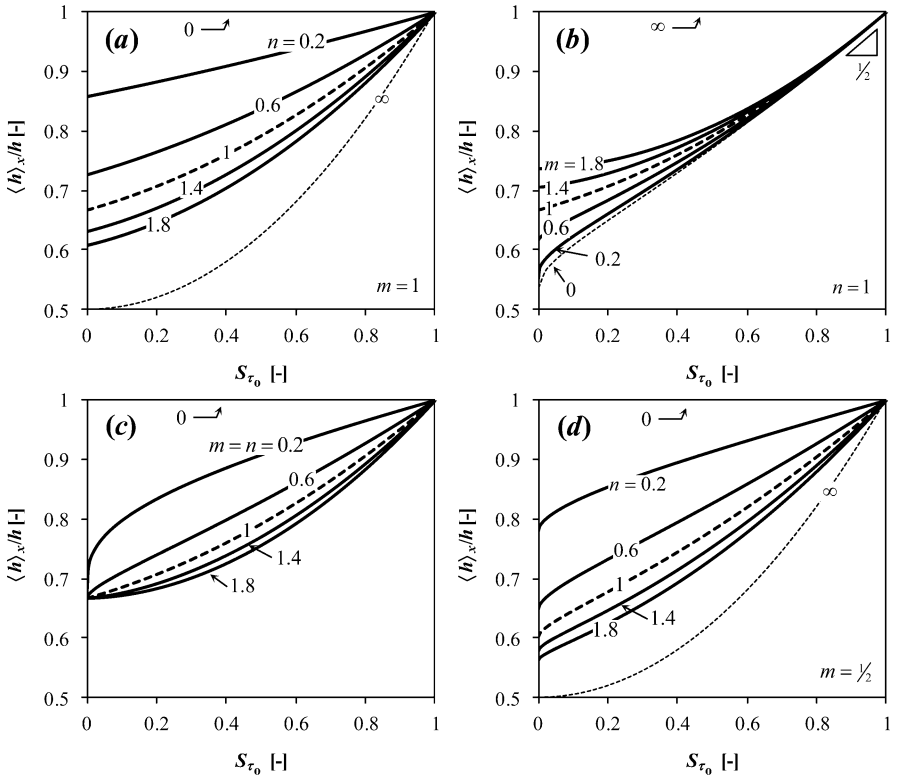

Figure 8. Ratio of the average film thickness to the local film thickness $\langle h\rangle_x/h$ as a function of S_{τ_0} for different values of (*a*) n (with $m = 1$) (i.e., Herschel–Bulkley case), (*b*) m (with $n = 1$), (*c*) $n = m$ (i.e., Heinz–Casson case) and (*d*) n (with $m = {}^1/_2$) (i.e., Herschel–Bulkley case). In panels *a*–*c*, the reference conditions were represented by a dashed line that correspond to a Bingham fluid (i.e., $n = m = 1$).

AUTHOR INFORMATION

Corresponding Author

*Tel.: +54 342 451 1595. Fax: +54 342 451 1079. E-mail: jmperalta@intec.unl.edu.ar.

Notes

The authors declare no competing financial interest.

ACKNOWLEDGMENTS

This research was supported partially by Universidad Nacional del Litoral (Santa Fe, Argentina), Consejo Nacional de Investigaciones Científicas y Técnicas (Argentina), and Agencia Nacional de Promoción Científica y Tecnológica (Argentina).

NOMENCLATURE

C = concentration, kg m^{-3}
Ca = capillary number ($\eta U\sigma^{-1}$)
${}_2F_1[a, b; c; s]$ = Gauss hypergeometric function
$\underline{g}$ = gravity acceleration vector, m s^{-2}
$|\underline{g}|$ = magnitude of $\underline{g}$ (9.81), m s^{-2}
g_x = component of $\underline{g}$ in x direction calculated by eq 10, m s^{-2}
$\langle h\rangle_x$ = average of h in x direction, m
h = local thickness of the film, m
h_L = h evaluated at L, m
K = consistency index used in eq 2, Pa s$^{n/m}$
L = length of the plate, m
m = second behavior index used in eq 2
N = number of samples
n = first behavior index used in eq 2
p = pressure, Pa
Q_z = flow rate per unit width, m^2 s^{-1}
rmse = root mean squared error defined by eq 15, m
S_K = ratio of the viscous stress to the maximum stress
S_{τ_0} = ratio of the yield stress to the maximum stress
T = temperature, K
t = time, s
t_d = draining time, s
U_p = velocity of the plate, m s^{-1}
$\underline{v}$ = velocity vector, m s^{-1}
$\langle v_x\rangle_y$ = average of v_x in y direction, m s^{-1}
v_x = component of $\underline{v}$ in x direction, m s^{-1}
$v_{x,max}$ = maximum value of v_x, m s^{-1}
x = position in x direction, m
y = position in y direction, m

Greek Symbols

$\dot{\underline{\gamma}}$ = rate of deformation tensor, s^{-1}
$|\dot{\underline{\gamma}}|$ = magnitude or second invariant of $\dot{\underline{\gamma}}$, s^{-1}
δ = position of the viscous to solid like behavior transition calculated by eq 9, m
η = apparent viscosity, Pa s
θ = angle between the axis of the plate and the axis of $\underline{g}$, deg
ρ = density, kg m^{-3}
σ = surface tension coefficient, N m^{-1}
$\underline{\underline{\tau}}$ = shear stress tensor, Pa
τ_0 = yield stress coefficient used in eq 2, Pa
ψ = function defined by eq 5

REFERENCES

(1) Jittavanich, K.; Clemons, C. B.; Kreider, K. L.; Aljarrah, M.; Evans, E.; Young, G. W. Modeling, Simulation and Fabrication of Coated Structures Using the Dip Coating Technique. *Chem. Eng. Sci.* **2010**, *65*, 6169.

(2) Tallmadge, J. A.; Gutfinger, C. Entrainment of Liquid Films—Drainage, Withdrawal, and Removal. *Ind. Eng. Chem.* **1967**, *59*, 18.
(3) Tu, Y.; Drake, R. L. Heat and Mass Transfer during Evaporation in Coating Formation. *J. Colloid Interface Sci.* **1990**, *135*, 562.
(4) Brinker, C. J.; Frye, G. C.; Hurd, A. J.; Ashley, C. S. Fundamentals of Sol-Gel Dip Coating. *Thin Solid Films* **1991**, *201*, 97.
(5) Lee, C. H.; Lu, Y.; Shen, A. Q. Evaporation Induced Self Assembly and Rheology Change during Sol-Gel Coating. *Phys. Fluids* **2006**, *18*, 052105.
(6) Patel, B. K.; Bhattacharya, S. Coating with Honey: A Study with Model Solids. *J. Food Process Eng.* **2002**, *25*, 225.
(7) Bhattacharya, S.; Patel, B. K. Simulation of Coating Process: Rheological Approach in Combination with Artificial Neural Network. *J. Texture Stud.* **2007**, *38*, 555.
(8) Yoo, S.-Y.; Jaluria, Y. Computational Study of Convective Transport in a Coating Applicator for a Non-Newtonian Fluid. *Numer. Heat Transf. Part Appl.* **2008**, *54*, 915.
(9) Ghorbel, D.; Barbouche, N.; Riahi, H.; Braham, A.; Attia, H. Influence of Fat Content on Rheological Properties of Molten Ice Cream Compound Coatings and Thickness of Solidified Products: Rheology and Thickness of Ice Cream Compound Coating. *J. Food Process Eng.* **2011**, *34*, 144.
(10) Spiers, R. P.; Subbaraman, C. V.; Wilkinson, W. L. Free Coating of a Newtonian Liquid onto a Vertical Surface. *Chem. Eng. Sci.* **1974**, *29*, 389.
(11) Kizito, J. P.; Kamotani, Y.; Ostrach, S. Experimental Free Coating Flows at High Capillary and Reynolds Number. *Exp. Fluids* **1999**, *27*, 235.
(12) Spiers, R. P.; Subbaraman, C. V.; Wilkinson, W. L. Free Coating of Non-Newtonian Liquids onto a Vertical Surface. *Chem. Eng. Sci.* **1975**, *30*, 379.
(13) Adachi, K.; Spiers, R. P.; Wilkinson, W. L. Free Coating of Viscoelastic and Viscoplastic Fluids onto a Vertical Surface. *J. Non-Newton. Fluid Mech.* **1978**, *3*, 331.
(14) Wichchukit, S.; McCarthy, M. J.; McCarthy, K. L. Flow Behavior of Milk Chocolate Melt and the Application to Coating Flow. *J. Food Sci.* **2005**, *70*, E165.
(15) Karnjanolarn, R.; Mccarthy, K. L. Rheology of Different Formulations of Milk Chocolate and the Effect on Coating Thickness. *J. Texture Stud.* **2006**, *37*, 668.
(16) Casson, N. A. A Flow Equation for Pigment−Oil Suspensions of the Printing Ink Type. In *Rheology of Disperse Systems*; Mill, C. C., Ed.; Pergamon Press: London, 1959.
(17) Peralta, J. M.; Meza, B. E.; Zorrilla, S. E. Mathematical Modeling of a Dip-Coating Process Using a Generalized Newtonian Fluid. 1. Model Development. *Ind. Eng. Chem. Res.* **2014**, DOI: 10.1021/ie500407t.
(18) Bird, R. B.; Hassager, O. *Dynamics of Polymeric Liquids I. Fluid Mechanics*; 2nd ed.; Wiley: New York, 1987; Vol. *1*.
(19) Mohos, F. Á. Appendix 3: Survey of Fluid Models. In *Confectionery and Chocolate Engineering*; Wiley-Blackwell: Oxford, UK, 2010; pp 582−605.
(20) Mizrahi, S.; Berk, Z. Flow Behaviour of Concentrated Orange Juice: Mathematical Treatment. *J. Texture Stud.* **1972**, *3*, 69.
(21) Herschel, V. H.; Bulkley, R. Konsistenzmessungen von Gummi−Benzollösungen. *Kolloid−Zeitschrift* **1926**, *39*, 291.
(22) Ostwald, W. Ueber Die Geschwindigkeitsfunktion Der Viskosität Disperser Systeme I. *Kolloid−Zeitschrift* **1925**, *36*, 99.
(23) Bingham, E. C. *Fluidity and Plasticity*; McGraw-Hill, 1922.
(24) Paez, T. L. Introduction to Model Validation. In *Proceedings of the IMAC-XXVII*; Curran Associates: Red Hook, NY, 2009.
(25) Peralta, J. M.; Chew, Y. M. J.; Wilson, D. I. An Analytical Method for Selecting the Optimal Nozzle External Geometry for Fluid Dynamic Gauging. *Chem. Eng. Sci.* **2011**, *66*, 3579.
(26) Martin, D. H. Functional Sensitivity Analysis of Mathematical Models. In *System Modeling and Optimization*; Drenick, R. F.; Kozin, F., Eds.; Lecture Notes in Control and Information Sciences; Springer: Berlin Heidelberg, 1982; pp 663−670.
(27) Ingalls, B. Sensitivity Analysis: From Model Parameters to System Behaviour. *Essays Biochem.* **2008**, *45*, 177.
(28) Reiner, M. *Deformation, Strain and Flow: An Elementary Introduction to Rheology*, 3rd ed.; H. K. Lewis: London, 1969.
(29) Ofoli, R. Y.; Morgan, R. G.; Steffe, J. F. A Generalized Rheological Model for Inelastic Fluid Foods. *J. Texture Stud.* **1987**, *18*, 213.
(30) Van Rossum, J. J. Viscous Lifting and Drainage of Liquids. *Appl. Sci. Res.* **1958**, *7*, 121.
(31) Tester, J. W. *Thermodynamics and Its Applications*; Prentice-Hall International Series in the Physical and Chemical Engineering Sciences; 3rd ed.; Prentice Hall PTR: Upper Saddle River, NJ, 1997.
(32) Chambon, G.; Ghemmour, A.; Laigle, D. Gravity-Driven Surges of a Viscoplastic Fluid: An Experimental Study. *J. Non-Newton. Fluid Mech.* **2009**, *158*, 54.
(33) Tallmadge, J. A. Withdrawal of Flat Plates from Power Law Fluids. *AIChE J.* **1970**, *16*, 925.
(34) Sylvester, N. D.; Tyler, J. S.; Skelland, A. H. P. Non-Newtonian Thin Films: Theory and Experiment. *Can. J. Chem. Eng.* **1973**, *51*, 418.
(35) Gutfinger, C.; Tallmadge, J. A. Films of Non-Newtonian Fluids Adhering to Flat Plates. *AIChE J.* **1965**, *11*, 403.
(36) Lee, S.; Ng, P. K. W.; Steffe, J. F. Effects of Controlled Mixing on the Rheological Properties of Deep-Fat Frying Batters at Different Percent Solids. *J. Food Process Eng.* **2002**, *25*, 381.
(37) Groenveld, P. High Capillary Number Withdrawal from Viscous Newtonian Liquids by Flat Plates. *Chem. Eng. Sci.* **1970**, *25*, 33.